

Recovery of a flawed hyperspectral imager calibration using optical modeling

William R. Johnson¹, Keith Hege², Dan O'Connell¹, and Eustace L. Dereniak¹

¹ Optical Sciences Center, University of Arizona,
1630 E. University Blvd., Tucson, Arizona 85721
wjohnson@optics.arizona.edu

² Steward Observatories, Department of Astronomy/Steward Observatory,
933 N Cherry Ave., Rm. N204, Tucson Arizona 85721-0065

Abstract: A reconstructed hyperspectral datacube has been successfully recovered from a badly flawed point-spread function (PSF) observation. The corrected PSF alleviated unnoticed detector saturation and misregistration artifacts in the calibration of a crucial, irreplaceable near-infrared flash hyperspectral imager dataset. This flawed PSF induced a defocus-like artifact as well as spectral distortions in the three-dimensional hyperspectral estimate of the data. The PSF artifacts, which would have caused severe misinterpretation of the spatio-spectral information, were correctable post detection using an optical model of the PSF constrained by the available flawed calibration.

©2004 Optical Society of America

OCIS codes: (040.3060) Infrared; (100.6950) Tomographic image processing; (300.6340) Spectroscopy, infrared.

References

1. M.R. Descour, C.E. Volin, E.L. Dereniak, T.M. Gleeson, M. F. Hopkins, D.W. Wilson, and P.D. Maker, "Demonstration of a computed tomographic imaging spectrometer using a computer generated hologram disperser," *Appl. Opt.* **36**, 3694-3698 (1997).
2. E. Tessar, "Image quality with current adaptive optics instruments," *Astron. Astrophys. Suppl. Ser.* **125**, 581-593 (1997).
3. C.R. Neyman, "Characterization of the AEOS Adaptive Optics System," *Astro. Soc. Of Pac.* **114**, 1260-1266 (2001).
4. M.R. Descour and E.L. Dereniak, "Computed-tomographic imaging spectrometer: experimental calibration and reconstruction results," *Appl. Opt.* **34**, 4817-4826 (1995).
5. J.P. Garcia and E.L. Dereniak, "Mixed-expectation image reconstruction technique," *Appl. Opt.* **38**, 3745-3748 (1999).
6. C.E. Volin, J.P. Garcia, E.L. Dereniak, M.R. Descour, T. Hamiltonian, and R. McMillian, "Midwave-infrared snapshot imaging spectrometer," *Appl. Opt.* **40**, 4501-4506 (2001).
7. C.E. Volin, "Portable snapshot imaging spectrometer," Ph.D. Dissertation (University of Arizona Press, Tucson, Arizona, 2000).
8. K. Hege, D. O'Connell, W. R. Johnson, S. Bastly and E. L. Dereniak, "Hyperspectral imaging for astronomy and space surveillance," in *Remote Sensing and Space Technology*, Proc. SPIE **5159**, 41-49 (2003).
9. J. Goodman, *Introduction to Fourier Optics* (McGraw-Hill, New York, 1996).
10. J.H.H. Barrett and K.J. Myers, "The Dirac Delta and other generalized functions," in *Foundations of Image Science*, (John Wiley & Sons, Inc., New Jersey, 2004), pp.63-94.
11. W.R. Johnson, K. Hege, D.O' Connell, and E.L. Dereniak, "Novel calibration recovery technique for an EM reconstruction," *Opt. Eng. Lett.* **43**, 10-12 (2004).

1. Introduction

Flash hyperspectral imaging (FHI) is the process of acquiring simultaneously a set of images of a particular scene in a number of relatively narrowband colors. Various scanning schemes of Fourier transform spectroscopy (essentially scanning in time) have been implemented for hyperspectral imaging. These methods have severe limitations in applications involving rapidly evolving scenes or on platforms with jitter. The non-scanning FHI avoids such undesirable blurring effects over the duration of data acquisition that occurs in scanning methods.

FHI is accomplished using a computed tomographic imaging spectrometer [1] (CTIS), a single instrument that performs spatial imaging of a scene while measuring the spectral content. It discretely samples a tomographic dispersion pattern formed by a computer-generated hologram (CGH) placed in the CTIS pupil. All of the information is acquired in a single exposure sufficiently short that no artifacts are caused by transient scene motion. A tomographic image is formed of the CGH projected field of view (FOV) on a conventional pixilated imager.

Observing with a large adaptive-optics [2] (AO) telescope, we used CTIS to recover the complete set of narrow band images for two points sources (a binary star) in a single integration. This provides hyperspectral imaging in a three-dimensional space. The spatial dimensions (x,y) correspond to the FOV of CTIS, confocal to the focal plane of the telescope. The third dimension is the wavelength (λ) of the scene irradiance. After spectral dispersion the pattern is re-imaged onto a focal plane array (FPA) and is stored on a local computer for post processing and reconstruction. CTIS uses indirect imaging techniques that require tomographic reconstruction of the limited-angle projections of the FOV produced by the CGH disperser. A generalized layout of CTIS can be seen in Fig. 1.

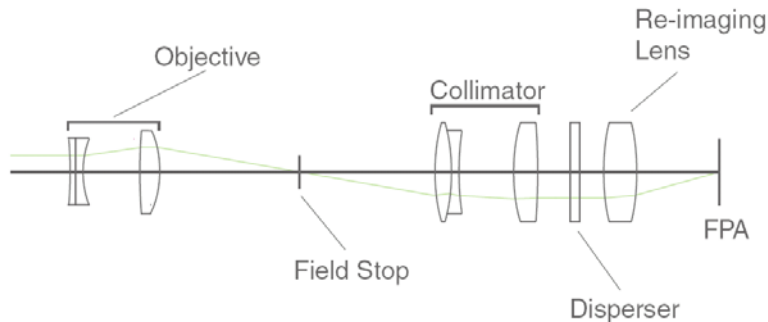


Fig. 1. The generalized graphical CTIS layout. The lens depictions are meant only to be representative of the role each lens plays in the system. The objective assembly in this work is the Air Force AEOS adaptive optics telescope.

2. Instrumentation

We used a large format, 1024x1024 pixel Mercury Cadmium Telluride (HgCdTe) array with an 18.5- μm pitch cooled to 77K and optimized for low-backgrounds. It has high quantum efficiency ($\eta > 60\%$) for our spectral bandpass (1150nm to 1960nm) and low ($< 5\%$) non-uniformity. The CGH was designed to have high dispersion, which allows for more spectral bands when imaged onto the large format FPA sensing compact support of the FOV. Our spectral resolution, defined by the calibration, is 10nm or 82 contiguous spectral bands. The 1mm square field stop is imaged onto the FPA at 1:1 magnification, so we end up with 54x54 pixel spatial sampling of the scene, giving similar finesse in all three directions.

The near-infrared CTIS is designed for astronomical objects, which we define as any object above the earth's effective atmosphere. We tested the capabilities of CTIS on luminous multiple point sources to evaluate our ability to reconstruct point-spread functions (PSF) accurately and to provide ease in object modeling for those astronomical observation

validation experiments. The 0.7" binary star HIP 98636 provides two PSF's with convenient separation in the FOV. A raw image from the CTIS is shown in Fig. 2.

Adaptive optics (AO) is a modern solution to atmospheric turbulence. With AO, ideally, the incoming aberrated wavefront is corrected by using a wavefront sensor, effectively consisting of a deformable mirror with fast electronics. Without AO the 0.7" separated components would be blurred together by the ~1" seeing limited for astronomical imaging. We used the Advance Electro Optical System [3] (AEOS) on Maui in Hawaii for these observations. The AEOS has a 3.67-meter diameter entrance pupil, which feeds the light to a Coudé path to the AEOS AO system, which has a 0.105-meter diameter exit pupil. We built a simple Cassegrain assembly to accept the collimated light (afocal beam) coming from the AO exit port and re-image it in the FOV of CTIS. Both the spatial and spectral resolution are limited by the spatial PSF. The optical PSF must be stable and close to optimal for tomographic reconstruction with $\lambda/2D$ per pixel resolution at 1 μ m. AEOS has state-of-the-art AO correction capabilities to insure this. The telescope is physically at high elevation (10,400 feet) to provide good seeing conditions to optimize AO performance. It is a continuing work of this project to devise methodology to compensate residual AO PSF effects on CTIS FHI.

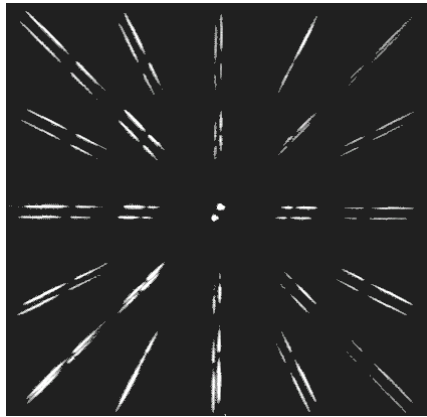


Fig. 2. Limited angle CTIS tomographic pattern of double star HIP 98636.

3. Technique

It is the purpose of this work to deal, post observation, with experimental difficulties encountered in acquiring data. The difficulties are two-fold.

1. The CTIS encountered unknown changes in its PSF due to an accident in transportation to the site. The CTIS camera was on a brief loan from Steward Observatory. In the process of delivery back to the continental United States, the camera and dewar system was altered substantially and could not be recovered in its former state.
2. The laboratory calibration itself was, unknown at the time, severely compromised by sensor saturation effects.

The following general forward mapping equation can describe CTIS

$$\mathbf{g} = \mathbf{H}\mathbf{f} + \mathbf{n}, \quad (1)$$

where \mathbf{H} is the transfer function, which represents the optical processing of the entire CTIS, AO and telescope. It describes the mapping process of the continuous 3D object onto the discrete sensor space. \mathbf{g} is the image of the target scene obtained by the FPA and \mathbf{n} is the usual noise vector. The correct interpretation of the spectrometer is a continuous-to-discrete mapping.

However, a discrete-to-discrete approximate mapping has been successfully used for past CTIS experiments [4,5]. Approximating the effect of the transfer function as a linear convolution operation described by $*$, the discrete model is

$$\mathbf{g}_m = \sum_{\lambda_b}^L \mathbf{H}_{\lambda_{b,n}} * \mathbf{f}_{\lambda_{b,n}} + \mathbf{n}_m, \quad (2)$$

$$1 \leq \mathbf{m} \leq \mathbf{M} \text{ and } 1 \leq \mathbf{n} \leq \mathbf{L},$$

where \mathbf{g}_m is an element of the row-ordered vector of observations \mathbf{g} , and $\mathbf{f}_{\lambda_{b,n}}$ is similarly an element of the row-ordered vector formed of the 2D estimates of the object \mathbf{f} corresponding to the passband λ_b seen in the CTIS FOV. It follows that once a system matrix is obtained, one can obtain the datacube, $\hat{\mathbf{f}}$, by multiplication of \mathbf{H}^{-1} with \mathbf{g} . This operation is inherently ill posed for CTIS, so advanced iterative reconstruction procedures [5] are used, such as expectation maximization (EM) and multiplicative algebraic reconstruction technique (MART), for the inversion. The limitations, and particularly the effects of violation of shift-invariance inherent in the convolution representation [Eq. (2)], are discussed in Ref. [8].

Although, the model [Eq. (1)] for CTIS defies direct PSF interpretation, in our useful PSF approximation of the transfer function \mathbf{H} , spectral and spatial data are multiplexed to represent the vector \mathbf{H} as a set of wavelength-dependent PSF segments, as shown by

$$\mathbf{g}_{\lambda_b} = \mathbf{H}_{\lambda_b}, \quad \lambda_1 \leq \lambda_b \leq \lambda_L \quad (3)$$

resulting from illuminating by $f_{\lambda_{b,n}} = \delta_{\lambda_{b,n}}$, a quasi-monochromatic point source formed at the output of a fiber optic. The resulting PSF datacube estimates the FOV discretely as a contiguous set $(\Delta x, \Delta y, \Delta \lambda)$ of volume elements, or voxels. Equation (3) shows how the calibration must quantitatively map each voxel onto the FPA. In principal, this mapping can store the wavefront aberrations, distortions, diffraction, and many other elements of the optical system. It is the quality of this mapping formation that came to question when a large amount of detector saturation was found to be present in the calibration, post data acquisition. Even more unfortunately, the obvious strategy of post-data acquisition recalibration was not possible for the project due to problems already stated.

Detector saturation is present when a large quantity of energy is incident onto the illuminated pixel of the detector. Saturation during calibration potentially occurs in spectral bands of high SNR based on detector integration times, source temperature and system throughput efficiency. When the charge build-up governed by the quantum efficiency of the detector exceeds a physical level, deemed the linear full well, the charge spills into adjacent optically active pixels, which are not saturated. Due to subtraction in the double scanning readout of the HgCdTe detector, this occurrence leaves a noticeable darkening of the central peak. The resulting saturated calibration PSF is shown in Fig. 3. This figure clearly shows the large bandwidth of saturation. This bandwidth is on the order of 10nm for each saturation PSF. Furthermore; the system potentially can lose multiple bands of spectral information given the spatio-spectral complexity of the CTIS reconstruction algorithm. Our HgCdTe detector has a full-well capacity of slightly over 100,000 electrons. The conversion gain can be adjusted to minimize saturation, but once the gain is exhausted, saturation occurs. This non-linearity produces in an apparent dark region in the PSF surrounded by wings. These artifacts of the PSF are caused by the procedure used to calibrate the CTIS. A large fiber is positioned in front of the CTIS and imaged onto the field stop. The fiber needs to be sufficiently large enough to obtain the required energy throughput, but in doing so causes multi-mode lobes from poor alignment. The fiber was adjusted to minimize these modes, although, some residual artifacts are still present. This PSF is stored in the laboratory measured voxel spread functions [Eq. (3)], which form \mathbf{H} . Although, it is known that the CTIS is not shift invariant, shift invariance is assumed [6,7] when obtaining the PSF's to avoid the

enormous inconvenience of obtaining [Eq. (3)] at each $\{x,y\}$ position in the FOV. Further study [8] has shown that an isoplanatic assumption yields image correlation of about 90% (Strehl ~ 0.9) over most of the free spectral range of CTIS.

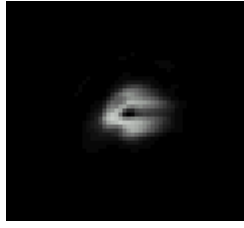


Fig. 3. Zoomed image of saturation energy leakage into surrounding pixels forming apparent PSF wings.

The CTIS is modeled as an incoherent imaging system, so the PSF only has meaning as the modulus of a complex function. The modulus can then be Fourier transformed to obtain the transfer function or non-normalized optical transfer function OTF [9]. Assuming a PSF with spatial extent given by $h(x,y)$, we obtain the OTF by

$$OTF = \iint_{\infty} |h(x,y)|^2 \exp[-i2\pi(\xi x + \eta y)] dx dy. \quad (4)$$

The CTIS saturated PSF will now be defined in terms of a collapsing Strehl ratio. We will simulate an idealized or diffraction-limited PSF using the measure of Strehl. We define our Strehl as

$$S_{sat} = \frac{\left\{ \iint_{\infty} OTF(\xi, \eta) d\xi d\eta \right\}_{saturated}}{\left\{ \iint_{\infty} OTF(\xi, \eta) d\xi d\eta \right\}_{diffraction_limit}} \quad (5)$$

where OTF is the optical transfer function as defined by [Eq. (4)]. It's basically the Fourier transform of the PSF modulus. The integral is over all spatial frequencies. It turns out that the modulation transfer function (MTF) is more interpretable, so the modulus of the OTF is taken to plot the resulting normalized spatial frequency MTF in Fig. 4. The left hand side of Fig. 4 shows the apparent defocus-like MTF for a saturated PSF in calibration. Both figures are shown normalized to unity energy in the PSF.

The idea underlining this work is to produce a constrained fit to “Strehl-match” the CTIS calibration with the AEOS optical system. After obtaining the OTF for the saturated and ideal image, it is integrated under the function [Eq. (5)] to obtain the theoretical Strehl ratio where the simulation is assumed to be aberration free. The PSF wings are taken into the account from conservation of energy arguments. A unit-less value of roughly 0.6 is obtained, which is consistent with a Strehl needing improvement. For this very reason, using the simulated image in place of the calibrated PSF will improve reconstruction performance with a Strehl constraint set to 0.6. Interestingly, recent reports have predicted Strehl for AEOS in the I-band of roughly 65%, which agrees well with the modeled value. The left hand side of Fig. 4 shows the optimal Strehl matching MTF based on the model of the AEOS optical system. The CTIS calibration is done without the AEOS system in place. As with every CTIS calibration, it's performed without the objective assembly. Every image reconstructed with our CTIS will be from the AEOS system, so it seems reasonable to match the Strehl from the CTIS calibration to what is expected for the CTIS and AEOS combination itself.

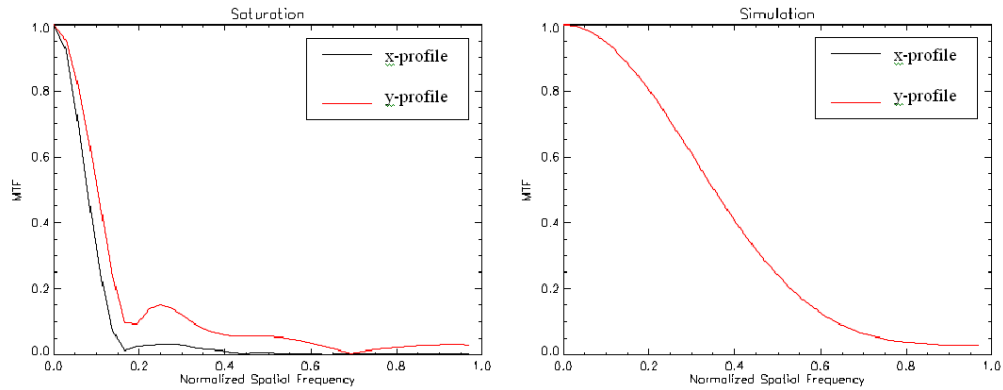


Fig. 4. MTF for saturation (L.) takes on appearance of a defocused MTF with an even number of Fresnel zones in these plots. Simulated MTF is also shown (R.).

A method for constraining the calibrator on a global level is devised so as to optimize the original energy information and not inject bias. We use the technique of limiting representations [10] as described by

$$\delta(x, y) = \lim_{k \rightarrow c} k \exp\left[-\pi k^2 (x^2 + y^2)\right], \quad (6)$$

where c is some relatively large but finite number determined by optimal fitting. A Gaussian distribution is assumed for the kernel function allowing our model to follow the central limit theorem. This is common for imaging when atmospheric aberration is present and provides ease in modeling with *canned* compliant packaged computer routines. It's also easily shown that this models the aberration free central lobe of an Airy disk rather well. The overall energy per voxel level is adjusted through Gaussian parameter optimization to fit the global constraint provided by the original calibrator images. This provides us with a self-consistent solution.

Each VSF is convolved with our limiting representation delta function of unit energy as described by [Eq. (6)], which in effect replaces each PSF with a Gaussian model of corresponding energy, retaining the photometric grating efficiencies as measured in the non-saturated wings at each locus. The previously determined empirical diffraction efficiencies are used to adjust the height of each Gaussian relative to the voxel frame. This is simply a multiplication operation. The maximum height will be determined along with the dispersion characteristic iteratively with an Energy Comparison Solver (ECS). The ECS performs the global integration by counting the energy in the original calibration frames while adjusting the size of the Gaussian parameters to obtain a minimized root-mean-square (RMS) distance.

This routine typically provided optimal fits within 8-iterations of the ECS. Taking advantage of the sparse nature of the \mathbf{H} , the gross artifact of saturation is eliminated as well as high order contributions (ghosting), and smearing by FPA characteristics. The new PSF's are constrained by energy, spatial position (x, y) , variance (σ_x, σ_y) , and covariance (σ_x^2, σ_y^2) in each PSF lobe in the ECS to approximate the original VSF energy. As noted earlier, a disadvantage of this technique is that the method assumes predetermined CTIS diffraction efficiencies. The diffraction efficacies are effectively found by empirical measures, which take into account the CGH spot efficiencies assuming a pseudo-impulse function input.

4. Results and conclusions

A successful exercise in post-data acquisition of the CTIS instrument calibration lost in an unexpected detection-to-source saturation of the system matrix has been demonstrated. Performing the specific tasks described by using the ECS creates an improved calibrator. Furthermore, the ECS allows improved spatio-spectral reconstructions. Constraining the calibrator via minimizing the RMS distance in a self-consistent fashion eliminates optically and electronically induced factors inherent in a faulty calibrator, which by and large increases spectral and spatial registration. Preliminary trials of this technique look promising as can be seen in the co-registered datacube rasters of Fig. 5. The left raster shows the large blurring or defocus-like appearance due to the saturated calibrator PSF. This is expected since spatial and spectral resolutions are interdependent on the calibrator PSF and since the MTF of Fig. 4 shows a defocus-like appearance. The defocus like effect is completely eliminated with this technique with excellent PSF enhancement as shown in the right raster.

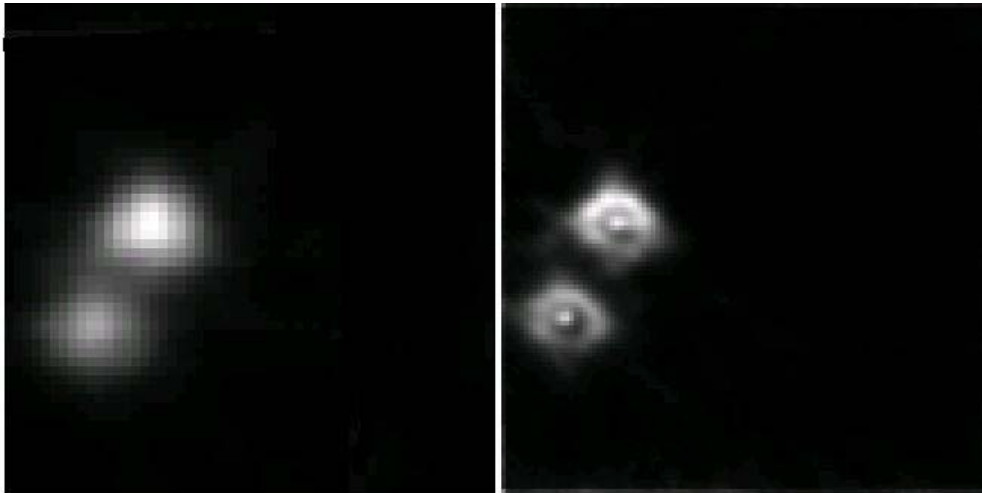


Fig. 5. Near-infrared co-registered reconstructed datacube grayscale raster showing before (L.) and after (R.) saturation correction.

The residual PSF spherical aberration-like artifact, which is still present on the right side of Fig. 5, is eliminated using a further post-data solver technique already described in the literature [11]. This technique further constrains the calibrator by applying a self-consistent least-squares approach to a physical misalignment in the CTIS itself during calibration. This further implementation allows the point source reconstructions to be at optimal fit with respect to the original data.

Acknowledgments

This work was supported in part by the National Science Foundation Award AST-0088598 with funding from the Air Force Office of Scientific Research, and utilized the AEOS facility of the Air Force Maui Space Surveillance